Experimental observation of a polarization vortex at an optical bound state in the continuum

-

Supporting Information

Hugo M. Doeleman,[1,2] Francesco Monticone,[3] Wouter den Hollander,[2] Andrea Alù[4,5,6] and A. Femius Koenderink[2,1,*]

[1] Van der Waals-Zeeman Institute, Institute of Physics, University of Amsterdam, Science Park 904, 1098 XH Amsterdam, The Netherlands

[2] Center for Nanophotonics, AMOLF, Science Park 104, 1098 XG Amsterdam, The Netherlands

[3] School of Electrical and Computer Engineering, Cornell University, Ithaca, NY 14853, United States of America

[4] Photonics Initiative, Advanced Science Research Center, City University of New York, New York, NY 10031, United States of America

[5] Physics Program, Graduate Center, City University of New York, New York, NY 10016, United States of America

[6] Department of Electrical Engineering, City College of The City University of New York, NY 10031, United States of America

[*] f.koenderink@amolf.nl

Linewidth narrowing and mode profiles of the TM mode

Figure S1a shows vertical crosscuts through Figure 1c in the main paper, calculated using rigorous coupled wave analysis (RCWA)[1]. The TM mode linewidth decreases strongly near the BIC condition around 720 nm wavelength. We verified that as one approaches the exact BIC condition, the quality factor diverges. Driving the system with an x-polarized plane wave very close to the BIC condition (720

nm wavelength, k_x/k_0 =0.446) and solving for the scattered field in a full-wave numerical simulation (COMSOL v5.3), we find a mode profile shown in Figure S1b. For modes with very large quality factor, the scattered field profile at the resonance condition is practically entirely determined by the contribution of only that mode (i.e., the TM mode). We recognize that a guided mode is launched in the grating, which decays away from the plane of the grating and shows very low leakage to propagating waves. A time-harmonic animation of this scattered field (provided as a separate supplementary file) shows that the wave is traveling in the backwards direction (whereas the incoming wave has positive k_x).

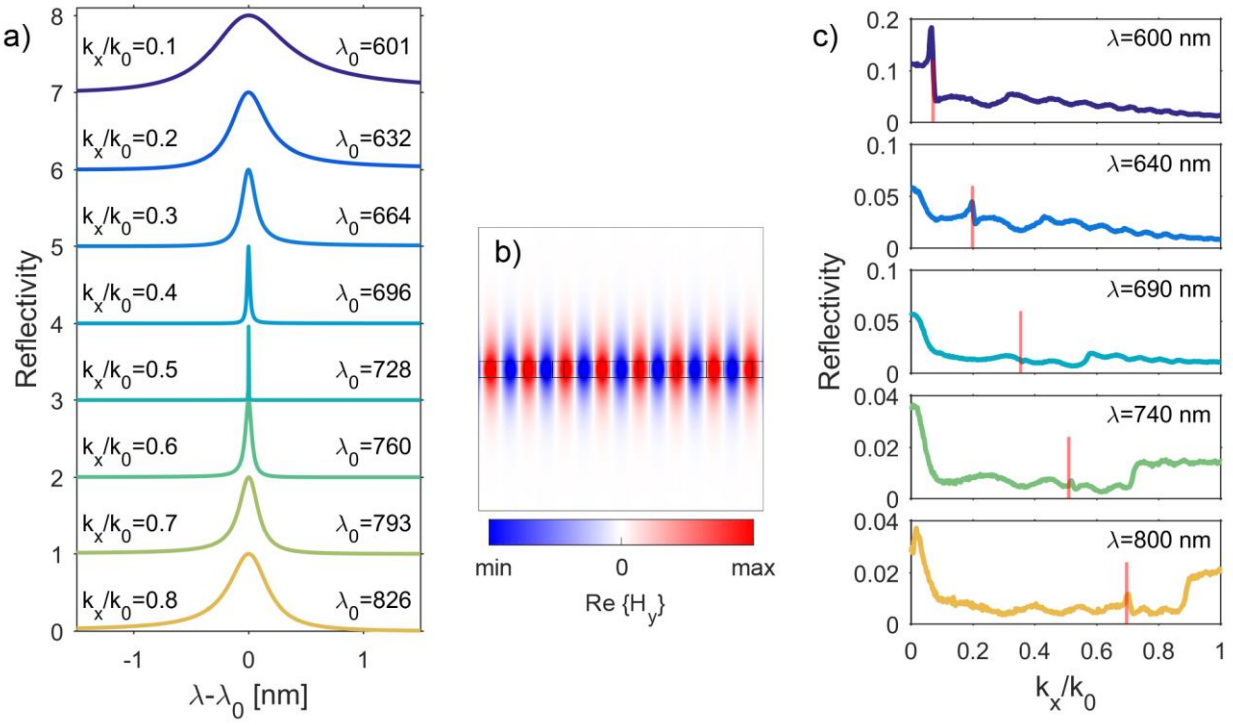

Figure S1: TM mode crosscuts and mode profile. (a) Calculated TM mode reflection spectra at fixed values of $k_x/\ k_0$ (indicated in the figure). We zoom in on a 2 nm region around the resonance wavelength λ_0 (also indicated). A strong decrease of linewidth is visible when approaching the BIC condition around 720 nm wavelength. **(b)** Field profile of the TM mode, driven by a plane wave with $k_x/\ k_0 =\ 0.45$ at 720 nm wavelength. We plot $Re\{H_y\}$ where H_y is the y-component of the scattered magnetic (electric) field by the grating. The TM mode is strongly bound to the grating slab. Black lines indicate material boundaries in the grating. **(c)** Measured reflection crosscuts at fixed wavelength, for horizontal input polarization. They correspond to horizontal slices from (the right side of) figure 1f in the main paper. Red lines indicate the position of the TM mode. We see a strong peak at low wavelength, which disappears around 690 nm, and reappears for higher wavelength.

Disappearance of the TM mode from the reflection

Figure S1c shows horizontal crosscuts taken from the reflection data in figure 1f in the main text, showing the disappearance of the TM mode as a feature in the reflectance. At wavelengths far below

690 nm, the TM mode is clearly visible as a sharp feature on top of the background, showing a Fano lineshape due to interference with this background. This feature fades out as we move towards the BIC wavelength, and reappears again for higher wavelengths.

Constructing the data cube

Our dataset consists of data cubes in k_x-k_y-wavelength-space. These are built up by projecting the back focal plane of the objective on the camera and acquiring images for a series of wavelengths. Three of such images are shown in Figure S2. A full data cube consists of 41 or 81 images for the measurements with y- and x-polarized input, respectively. Since the objective back focal plane is circular, the data cubes actually assume a cylindrical shape. We refer to the supplementary videos for an animation of two entire data cubes at x- and y-polarized inputs.

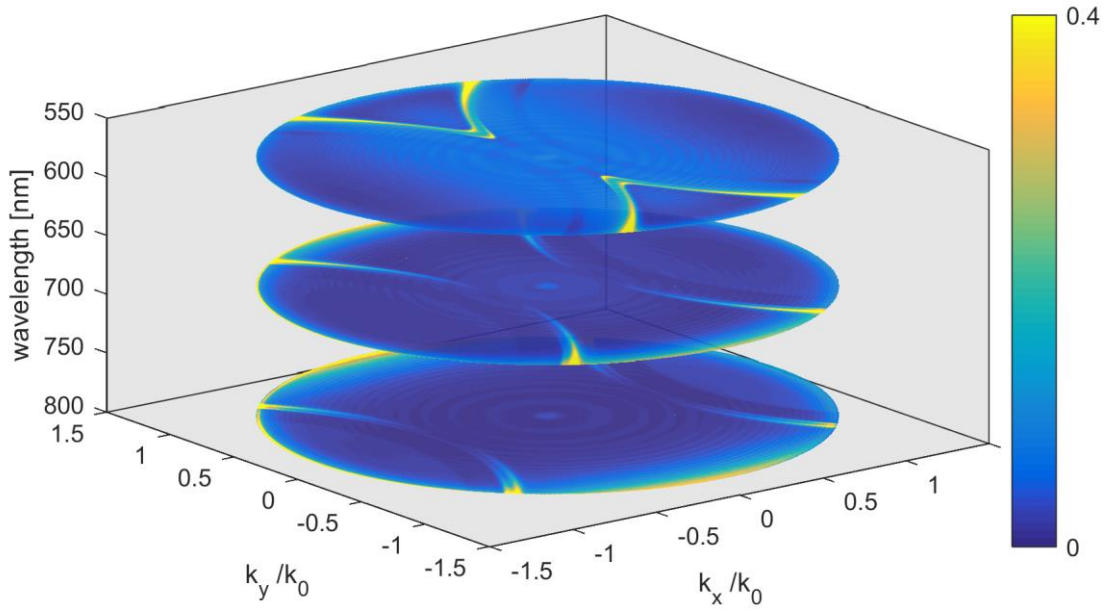

Figure S2: Crosscuts through one of the data cubes, taken at 670, 680 and 790 nm. The images show reflectance of our sample under x-polarized input polarization, normalized to a gold mirror. We clip the color scale for better visibility of the leaky modes.

Additional polarimetry results

Figure S3 and S4 show single-wavelength images of the reflected intensity and polarization angles for x- and y-polarized inputs, respectively. Figure S3 demonstrates that the modes show a clear signature not only in polarization main axis angle α, but also in ellipticity angle χ. In Figure S4, one can observe that the same trends are visible if the input light is switched from x- to y-polarization: The modes are clearly

visible and we can see α switch quadrants around 690nm, the wavelength of the BIC. A notable difference is that the TM mode signature disappears close to the x-axis, due to polarization mismatch. The TE mode is dominant throughout most of k-space for y-polarized input, as this mode is better matched to the input polarization and is naturally brighter due to the absence of a BIC.

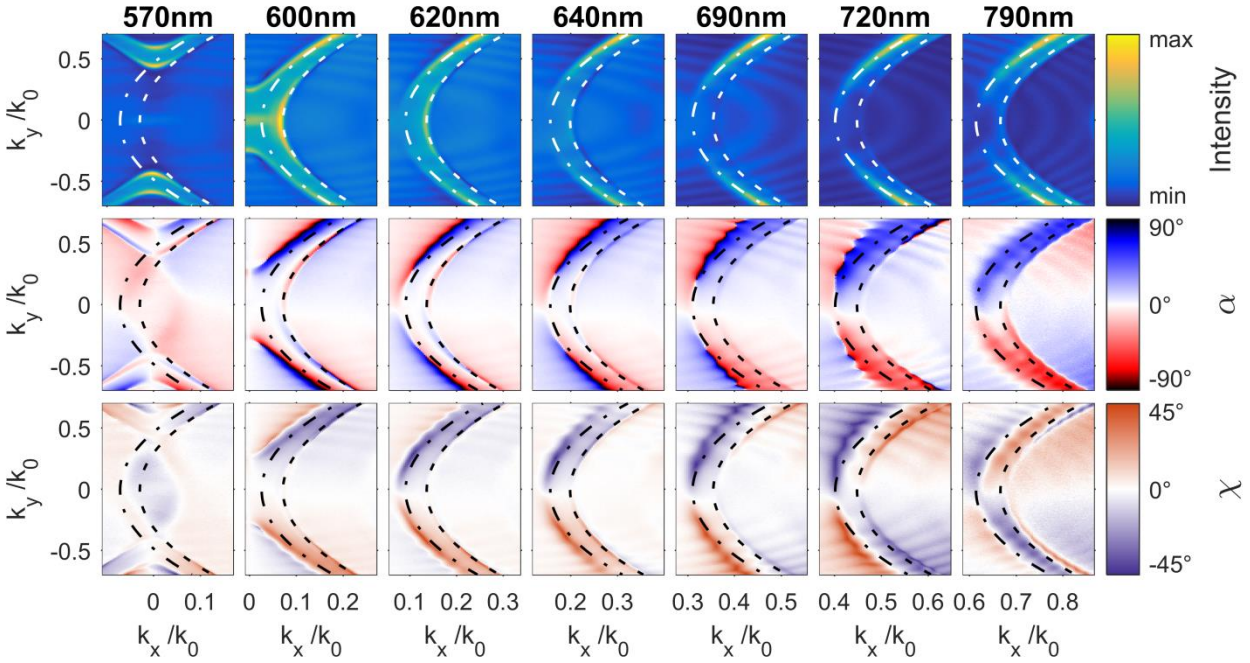

Figure S3: Zoomed-in images of the sample reflection, showing intensity and polarization angles α and χ. Input polarization was along the x-axis. The first two rows display the same data as Figure 2 in the main paper. The dashed lines indicate the fitted dispersion of the TM (right, dashed ellipse) and TE (left, dash-dotted ellipse) modes. Both display clearly distinct features in the maps of α and χ. Intensity minima (in camera counts) in the top row images are (from left to right) [5, 3, 11, 18, 16, 15, 5] and the respective maxima are [224, 231, 268, 375, 558, 680, 155].

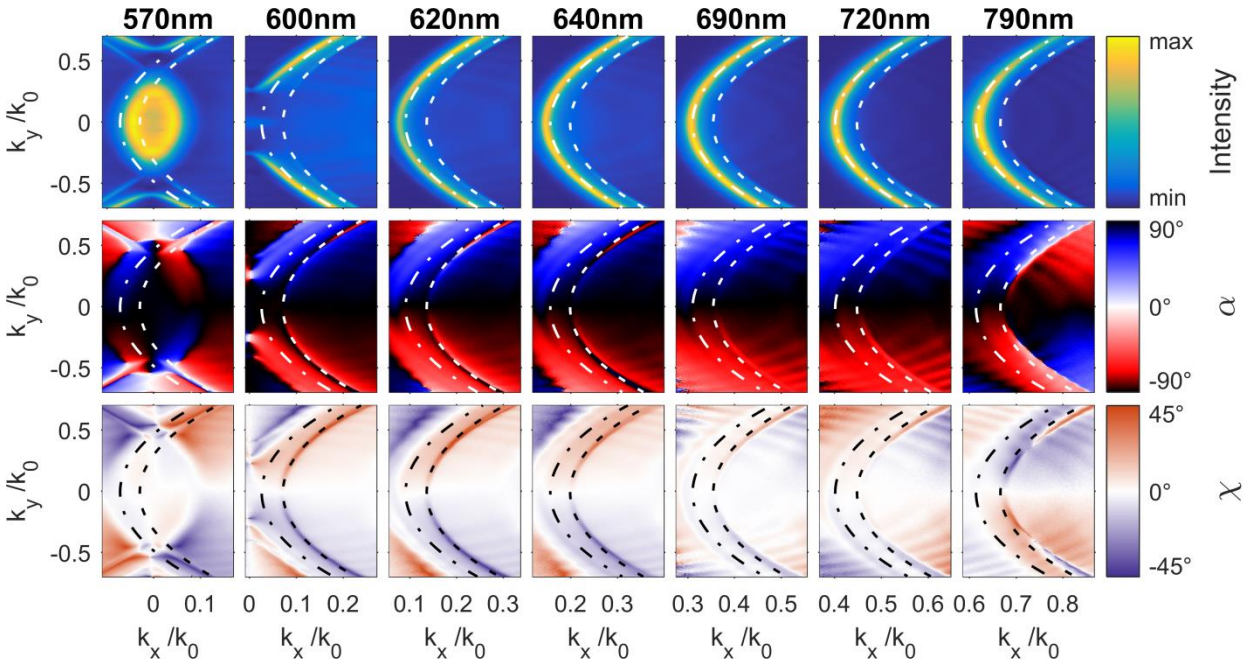

Figure S4: Reflected intensity and polarization angle images, now with input polarization along the y-axis. Again, the dashed lines indicate the fitted dispersion of the TM and TE modes. Importantly, the same dispersion relation was used for both the data with x-polarized and with y-polarized input. In these images the TE mode dominates, and the TM mode is invisible on the x-axis due to an orthogonal input polarization. Nevertheless, one can see the same behavior for α and χ of the TM mode as for x-polarized input: both change sign around the wavelength of the BIC, indicative of the vortex. Intensity minima (in camera counts) in the top row images are (from left to right) [1, 1, 8, 3, 1, 3, 1] and the respective maxima are [908, 896, 1348, 1399, 1770, 1808, 850].

Figure S5 shows the collapsed-resonance images of α and χ of the TM and TE modes, now for y-polarized input light. The same dispersion relation was used to produce these plots and those in Figure 3 of the main paper. We can see the vortex clearly in the plot of α: e.g. in the upper left quadrant, α changes from red to blue with increasing k_x. Note that this transition does not occur close to the x-axis, since there the TM mode disappears and the reflected signal is dominated by the background and the TE mode. In the χ map we can see a similar crossing of nodal lines as in Figure 3 of the main paper, with the difference that the sign of χ (i.e. polarization handedness) has flipped. This is to be expected, since the ellipticity in reflection arises from the addition of TM reflection and a background contribution. If the TM contribution remains constant in polarization and the background changes from nearly x-polarized to y-polarized, the sign of handedness flips. For the TE mode, we see a clear absence of a vortex in the map of α. We can observe a slight handedness in the χ map, much weaker than for the TM mode because the TE mode reflection is far stronger than the background. A similar crossing of nodal lines as in the TM map is faintly visible, which we attribute to the TM mode forming a very weak background to the TE mode, leading to a trace of its ellipticity being visible in the TE map.

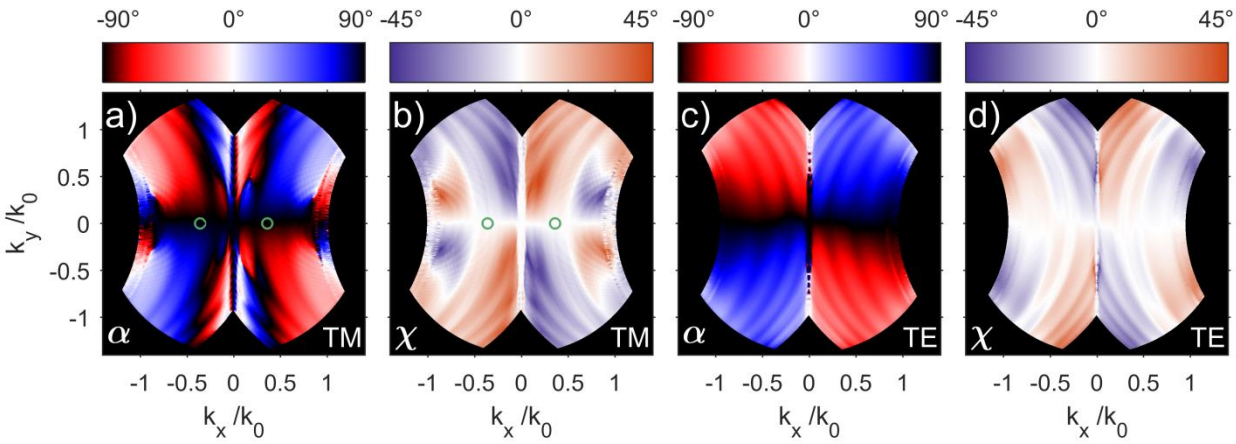

Figure S5: Collapsed resonance plots tracing polarization properties over the leaky-wave dispersion surface, for y-polarized input light. As in Figure 3 of the main paper, we show polarization angles α (Panel a and c) and χ (Panel b and d) for the TM (Panels a,b) and the TE mode..

Polarimetry obtained from RCWA

Figure S6 shows single-wavelength k-space images of the intensity and polarization of the grating reflection, obtained from RCWA calculations. We used the same grating as for figure 1c in the main paper, except that we added a small index difference between the top (n=1.517) and bottom (n=1.46) medium to account for the finite background reflection in our measurements. We see very good qualitative agreement with the experimental data in figure 2b of the main paper. The TM mode switches polarization around 720 nm, which is the BIC wavelength here.

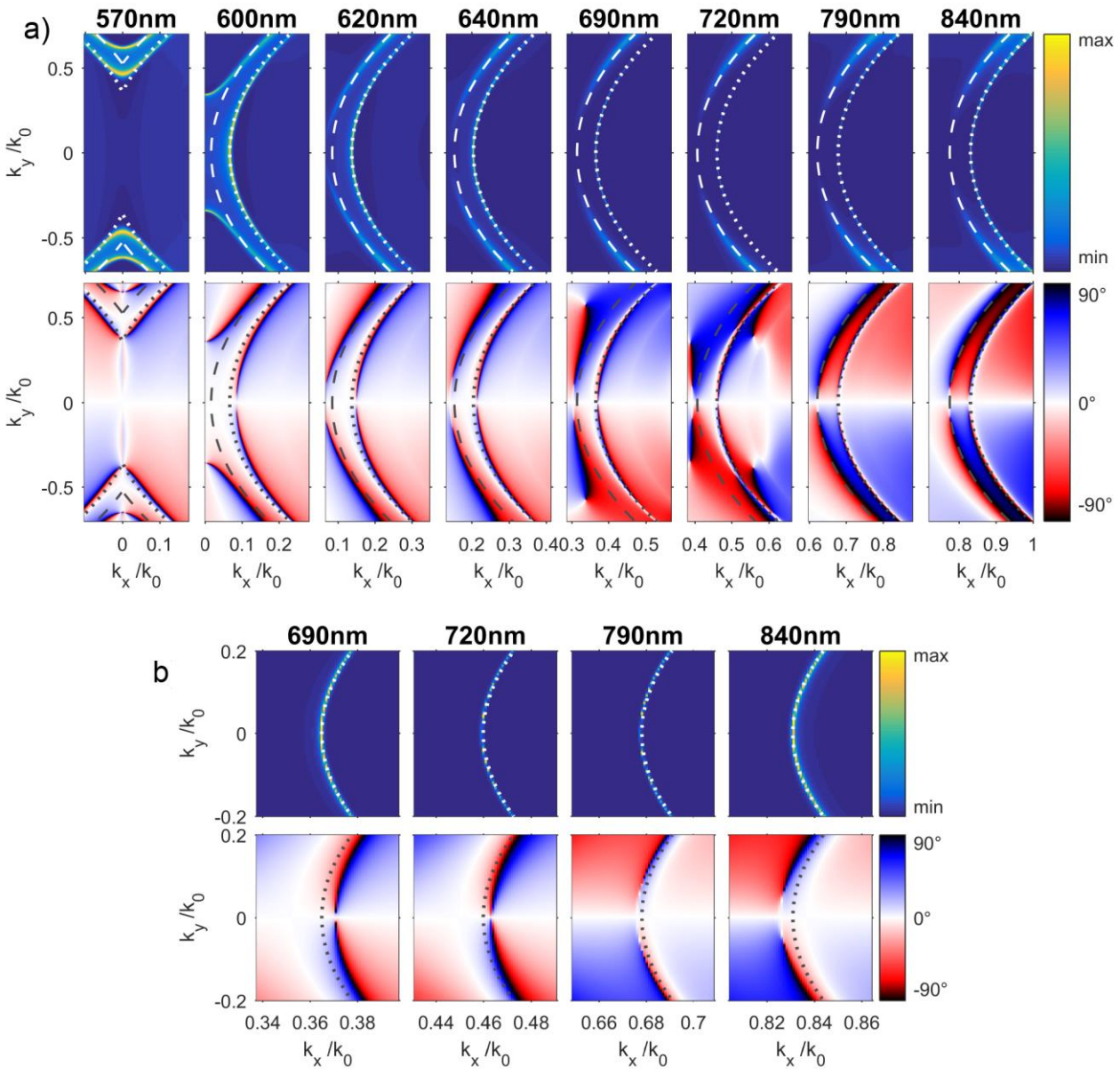

Figure S6: Single-frequency shots obtained from RCWA. (a) Calculated intensity (top row) and polarization angle α (bottom row) of the grating reflection. The dashed lines indicate the fitted dispersion of the TM (dotted ellipse) and TE (dashed ellipse) modes. We see a switching of polarization angle around the BIC wavelength (720 nm). Note that we show the same wavelengths as in fig. 2 of the main paper and fig. S3 and S4, except for the extra shot at 840 nm wavelength. The latter was added to show more clearly the polarization switching, because the theoretical BIC lies at somewhat higher wavelength than the experimental. **(b)** Zoomed-in images at the highest 4 wavelengths in panel a, which support very narrow TM modes. We zoom in on the region where the TM mode crosses the x-axis, to show more clearly the switching of polarization around the BIC wavelength.

Analysis of dipole contributions to the polarization of the grating unit cell

To understand the interference that lies at the heart of the bound state in our sample, we study the polarization induced in the unit cell of the grating. We will use this information in the next section to set up an electromagnetic dipole model. Using full-wave numerical simulations (COMSOL v5.3), we excite the grating at an angle and wavelength (710 nm) very close to the BIC. We then decompose the induced

polarization currents in the unit cell into their multipolar contributions. Throughout this work, we use units for electric and magnetic fields, dipole moments and polarizabilities as defined in earlier electromagnetic point scattering work[2]. This facilitates comparison between electric and magnetic components, since in this unit system electric and magnetic dipoles have the same units and an electric and a magnetic dipole of equal strength radiate an equal total amount of power.

Figure 4c in the main text shows the contributions from the 3 induced electric and magnetic dipoles, evidencing that the z-oriented electric and the y-oriented magnetic dipoles p_z and m_y are dominant. Figure S7 shows the grating reflectivity, induced dipole moments p_z, m_y and p_x (per unit length), the ratio between p_z and m_y and the phases of these dipoles and the driving fields, as k_x is scanned over the resonance condition near the BIC. We find that p_z and m_y are in phase, despite the fact that the corresponding driving fields are π out of phase, indicating that effective electric z-polarizability and magnetic y-polarizability are π out of phase. At the resonance, we find a ratio of $\frac{m_y}{p_z} = 0.48$. We will use this ratio and phase relation as input for the dipole model in the following section.

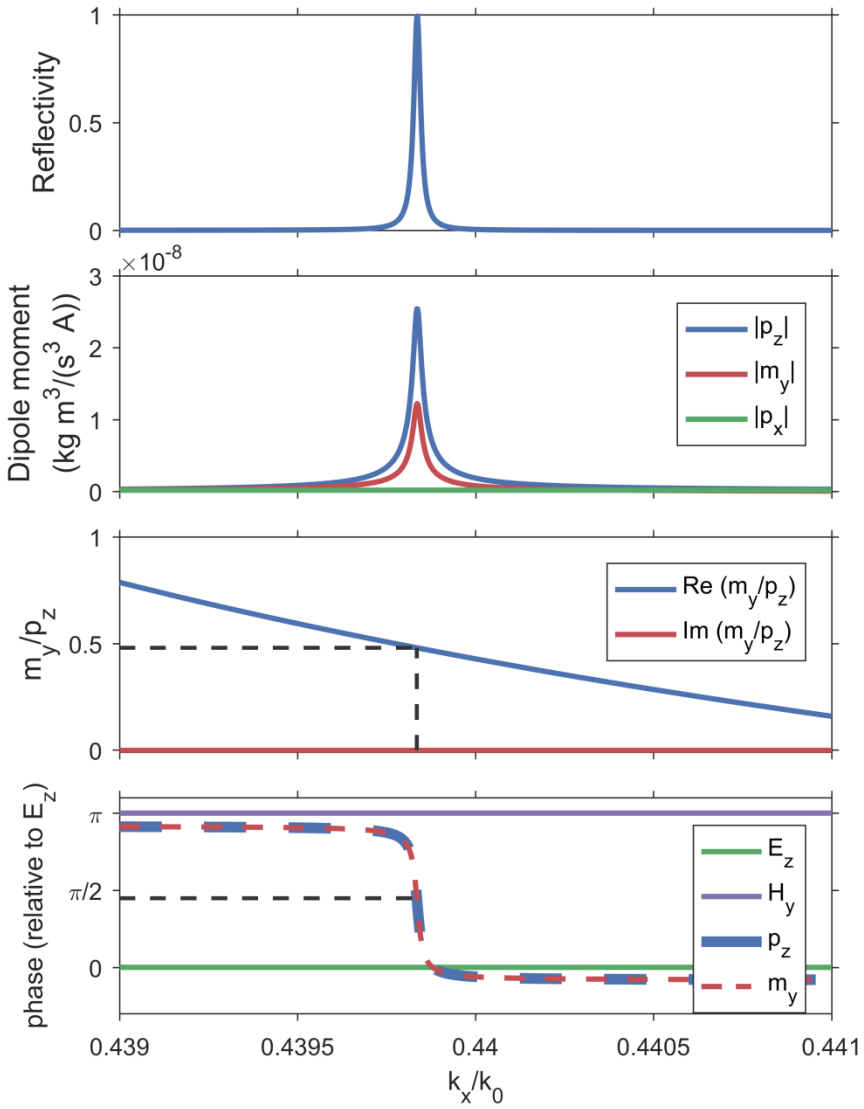

Figure S7: Full-wave numerical calculations of the induced dipoles in the grating unit cell. Calculated grating reflectivity, induced dipole moments p_z, m_y and p_x, the ratio between p_z and m_y (real and imaginary parts) and the phases of these dipoles and the driving fields, as function of in-plane momentum k_x/k_0 of an incident plane wave. Reflectivity and dipole moments peak as the incident wave is scanned over the resonance condition, and m_y/p_z equals 0.48 here. Note that the imaginary part of m_y/p_z is 6 orders of magnitude smaller than its real part. Moreover, we find that p_z and m_y oscillate in phase. Dipole moments are per unit length.

Far-field interference in an electromagnetic dipole model

We use an electromagnetic dipole model to qualitatively describe the origin of the bound state in our grating. We first consider radiation by a constantly oscillating dipole in Figure S8, showing that the combination of dipoles found in our grating unit cell leads to a node in the radiation pattern and a corresponding vortex in polarization. Then, to better compare to our measurements, in Figure S9 we let the dipole be driven by a plane wave and study the specular reflection. This allows the addition of a non-resonant interface reflection, present in any realistic measurement. We show that the combination of

this reflection and a contribution that mimics the TE mode reflection can reproduce qualitatively the results from our measurements. Note that these single-dipole calculations have as a major advantage that maps like those in Figure 3 in the main paper and Figure S5 can be calculated easily without tracking of a leaky waveguide mode, as needed in the experimental data. To facilitate comparison to our experiment, all calculations are done for a dipole exactly at an interface ($z = 0$) between two media of refractive index 1.5 (top) and 1.45 (bottom). Driving plane waves come from the top medium, and the radiation and reflection are monitored in the top medium as well. Far-fields radiated by the dipole are calculated according to

$$\vec{E}_{FF}(\theta, \phi) = \overleftrightarrow{G}(\theta, \phi) \cdot \vec{p}\,, \qquad (1)$$

where $\vec{E}_{FF} = \left(E_x, E_y, E_z, H_x, H_y, H_z\right)$, $\overleftrightarrow{G}(\theta, \phi)$ is the Green function for a dipole near an interface in the angular spectrum representation[3] and $\vec{p} = \left(p_x, p_y, p_z, m_x, m_y, m_z\right)$ is the electromagnetic dipole moment. The calculated far-fields are transformed to the back-focal-plane (BFP)of an ideal objective to create images that can be compared to our measurements. We took the free-space wavelength to be 700 nm.

Figure S8 shows the radiation patterns of a z-oriented electric dipole p_z (a-b), a y-oriented magnetic dipole m_y (c-d) and the coherent sum of the two (e-f), where we have chosen $p_z = 1$ and $m_y = 0.5$, in accordance with the dipole strengths and orientations found in our grating unit cell. The individual dipoles display a simple dipolar radiation pattern. The sum of the two shows a directional emission pattern, and in fact combinations of electrical and magnetic dipoles have been known to show directionality[4,5]. The emission pattern shows a node that coincides with a vortex in polarization angle α and occurs at nonzero k_x. The location of this node can be tuned using the ratio of p_z and m_y: a stronger magnetic component shifts the node outward, until it reaches the edge of k-space (i.e. grazing angles) exactly at $m_y/p_z = n$, where n is the index of the surrounding medium. This is similar to the famous Kerker condition[6], with the exception that the dipole is at an interface. A negative ratio flips the node location to the left half-space. Note that this behavior is reminiscent of the results of Zhen et al.[7], where it was shown that BICs in dielectric gratings shift their location if the system parameters, e.g. grating fill fraction, are changed. Such changes would also change the relative contributions of electric and magnetic dipole components to polarization currents.

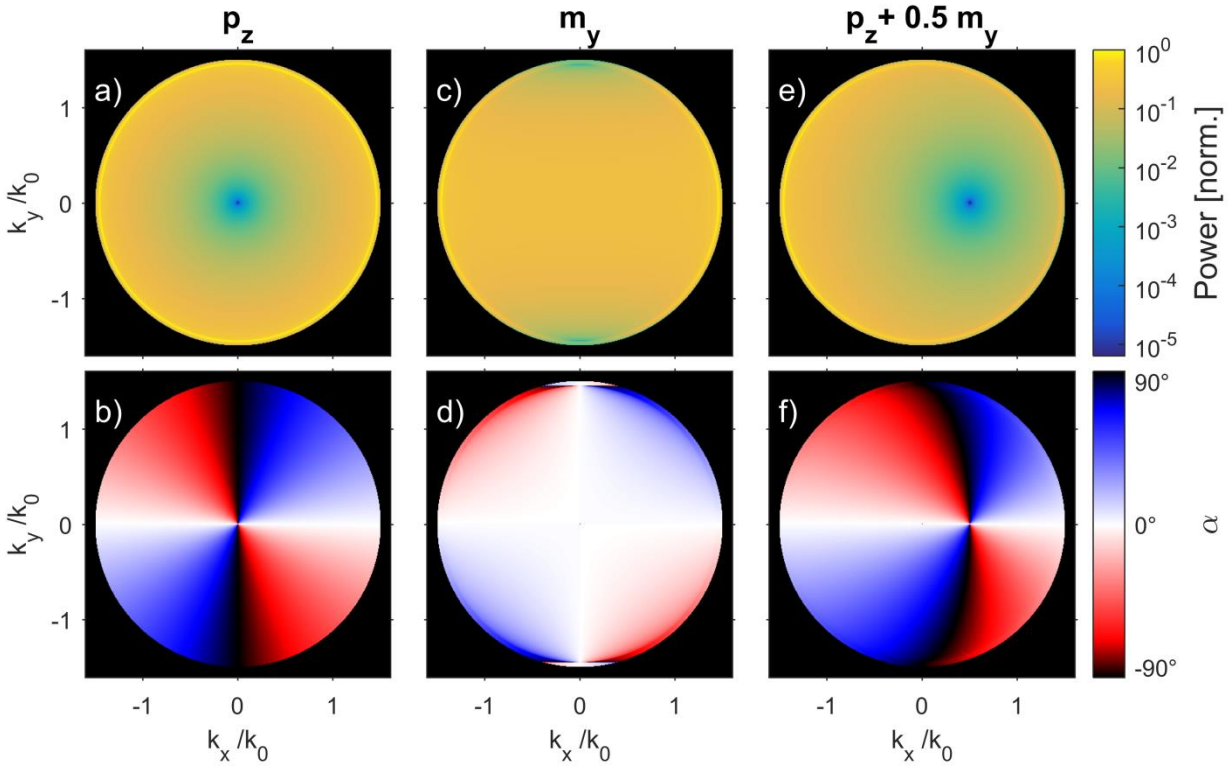

Figure S8: Intensity and polarization of electromagnetic dipole emission patterns. We show k-space images of the radiated power (top row) and polarization angle α (bottom row) by a z-oriented electric dipole p_z (a-b), a y-oriented magnetic dipole m_y (c-d), and the sum of the two, with $p_z = 1$ and $m_y = 0.5$. Panels e-f show a node at a non-high-symmetry point that coincides with a polarization vortex. Radiated power maps in the top row are normalized to their maxima.

Driven dipoles and the role of the background reflection

To better mimic the conditions in our experiment, we now drive the dipoles by a plane wave, rather than letting them oscillate at a fixed magnitude. We consider a non-diffractive sheet of non-interacting dipoles, in which the response of the sheet is simply given by the response of the single particle times the particle density[8]. We then monitor the reflected light in the specular direction. The induced dipole moment in the single dipole can be described as $\vec{p} = 4\pi\epsilon \cdot \overleftrightarrow{\alpha} \cdot \vec{E}_{in}(\vec{r}_0)$, where ϵ is the permittivity of the upper medium, $\overleftrightarrow{\alpha}$ is a 6-by-6 electromagnetic polarizability tensor [Sersic2011point], and $\vec{E}_{in}(\vec{r}_0)$ is the 6-element vector containing the electric and magnetic fields at the location $\vec{r}_0$ of the dipole. We take $\overleftrightarrow{\alpha}$ to be a diagonal matrix, with the diagonal elements $(\alpha^p_{xx}, \alpha^p_{yy}, \alpha^p_{zz}, \alpha^m_{xx}, \alpha^m_{yy}, \alpha^m_{zz})$ determining the electric and magnetic polarizability along each axis. The total reflected fields in the specular direction (θ_s, ϕ_s) are then given as

$$\vec{E}_r = \vec{E}_{r,BG}(\theta_s, \phi_s) + \rho\, \overleftrightarrow{G}(\theta_s, \phi_s) \cdot \vec{p}\,, \qquad (2)$$

where $\vec{E}_{r,BG}(\theta_s, \phi_s)$ describes the background contribution due to reflection at the interface, and ρ being the particle density. The second term describes the light emitted by the dipole in the specular direction, similar to Equation 1. Driving plane waves are taken to be x-polarized in the BFP of the ideal

objective, and we subsequently transform them to waves in the sample plane. The total reflected fields are again transformed back onto the BFP, as was also done for Figure S8.

Figure S9 shows k-space images of reflection magnitude and polarization angles α and χ for an electromagnetic dipole with and without background terms. For Figure S9 a-c, we use $\rho = 100\,\mu m^{-2}$ and take all elements of the polarizability $\overleftrightarrow{\alpha}$ to be zero, except $\alpha_{zz}^{p} = 1.5 \cdot 10^{-2}\,nm^3$ and $\alpha_{yy}^{m} = -0.1\,\alpha_{zz}^{p}$, leading to induced p_z and m_y dipoles only. The numbers were chosen such, that a plane wave incident under an angle close to that of the BIC induces p_z and m_y dipoles with a ratio as found in the grating unit cell. We see a similar behavior as in Figure S8c, with a node in reflection on the positive x-axis coinciding with a vortex in polarization angle α. However, a copy of this node can now be found on the negative x-axis. This is because, if the driving plane wave propagation direction is mirrored in the y-axis, the relative phase between its E_z and H_y components is changed from π to 0. This leads to a reversed sign in the relative phase of the induced dipoles p_z and m_y which, as mentioned in the previous paragraph, puts the node in the other half-space. Figure S9b reminds strongly of the type of polarization profile predicted by Zhen et al.[7] for similar structures, and is qualitatively similar to our measured polarization profile. Also note in Figure S9c that the polarization is linear, in accordance with theoretical predictions[7].

Figure S9d-f show the case where additional polarizability elements $\alpha_{yy}^{p} = 1i\,\alpha_{zz}^{p}$ and $\alpha_{zz}^{m} = 0.2i\,\alpha_{zz}^{p}$ added to the polarizability tensor, to qualitatively mimic the TE mode in the experiment. It was found that illumination of the grating with an s-polarized plane wave at the TE resonance condition, led to a dominant y-polarized electric dipole p_y and a weaker in-phase z-polarized magnetic dipole m_x. It can be seen in Figure S9d-f that the presence of the TE mode does not destroy the nodes, as it is not excitable by x-polarized plane waves on the k_x axis, and that the map of angle α is not strongly affected near the BICs. However, the interference between the vortex contribution of p_z and m_y on the one hand, and the out-of-phase p_y and m_x contributions on the other hand, lead to a non-zero ellipticity with a crossing of two nodal lines at the vortex, as shown in Figure S9f. Such a crossing was also observed in Figure 3 of the main paper. Note that p_y and m_x do not necessarily need to be $\pi/2$ out of phase with α_{zz}^{p} to achieve this effect, as chosen here. It simply needs to have a phase difference $0 < \Delta\phi < \pi$.

In the experiment, a weak non-resonant reflection from the oil-glass interface is also expected to influence the polarization. Figure S9g-i show the case where, on top of the three dipolar contributions in panel d-f, the non-resonant Fresnel reflection $\vec{E}_{r,BG}(\theta_s, \phi_s)$ from the interface was added. We see that this makes the nodes disappear, and the vortices in α changes to a profile that strongly resembles our results from Figure 3a in the main paper. Also, the crossings of the nodal lines in the map of χ remain, shifting slightly outward from the locations of the vortices, as was also observed in Figure 3b and Figure S5b.

In conclusion, we have performed calculations of the radiation from and reflection of an electromagnetic dipole. Results showed angular intensity and polarization maps that strongly resemble our experimental results on the grating containing a BIC. This provides a novel, simple and intuitive explanation for the presence of a BIC in these type of gratings, based on the interference between two radiation modes in

the unit cell of the grating. Moreover, through this model we were able to explain the surprising nodal line crossings in the maps of ellipticity angle χ observed in the experiment. These can arise due to the interference of light from the TM mode, containing the vortex, with light from the TE mode and a non-resonant background reflection.

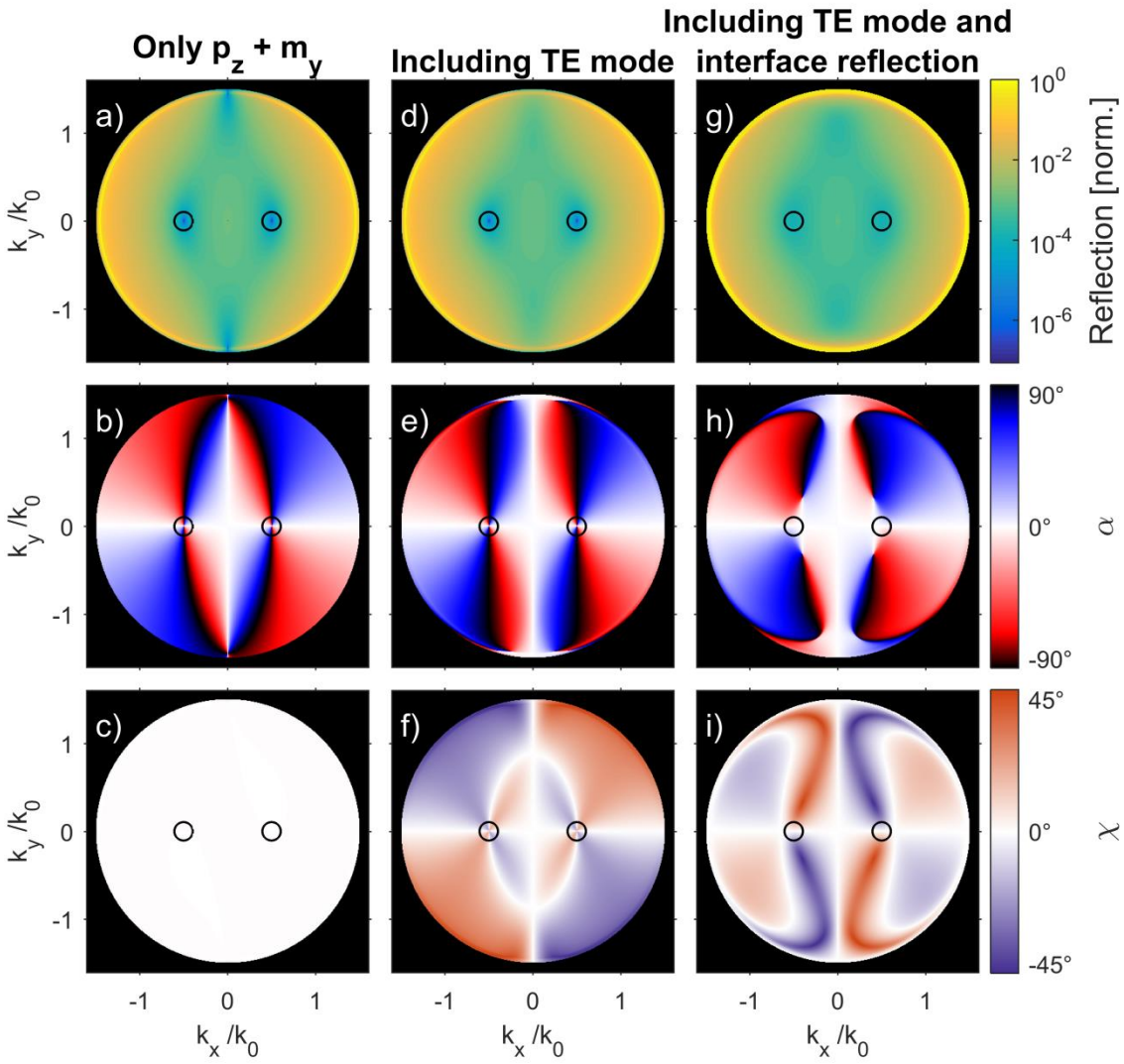

Figure S9: The effect of a background to the polarization feature of a BIC. K-space images of the reflected power (top row), polarization angle α (middle row) and ellipticity angle χ (bottom row) from a sheet of electromagnetic dipoles. **(a-c)** Dipoles with non-zero polarizability elements α_{zz}^{p} and α_{yy}^{m}, with two BICs left and right of the origin. **(d-f)** Dipoles with the same non-zero polarizability elements α_{zz}^{p} and α_{yy}^{m} as in (a-c), but with additional non-zero elements α_{yy}^{p} and α_{zz}^{m}, where the last two elements are used to model the TE mode. **(g-i)** Same dipoles as in (d-f), now also including a non-resonant reflection contribution from the interface. Reflection maps are normalized to their maxima.

Charge bouncing

An interesting prediction by Zhen et al.[7] is that, since topological charge is a conserved quantity, vortices with charges of the same sign can bounce as the geometrical parameters of the system are varied. This

effect is also visible in our simple dipole model. A change in e.g. grating thickness would lead to a change in the relative strengths of the dipole contributions to the polarization currents in the grating. We can mimic this by changing the relative dipole strength in our model. The vortices studied previously do not bounce but instead slowly converge towards the origin for increasing electric dipole strength. However, also other combinations of dipoles can show vortices. In Figure S10 we show intensity and polarization plots for a sheet of dipoles with 3 different combination of x-oriented electric polarizability $\alpha_{xx}^{p}$and y-oriented magnetic polarizability α_{yy}^{m}. The dipoles are located in a medium of index 1.5. Note that this combination of dipoles is aligned with the fields of a TM mode on the x-axis, and could thus describe vortices in TM-like modes. For $\alpha_{yy}^{m}/\alpha_{xx}^{p} =$ -1.2, we see 2 polarization vortices of charge +1 on the x-axis coinciding with nodes in reflection. As we change the relative strength, the vortices move to the Γ-point and subsequently 'bounce' to opposite sides on the y-axis. This is exactly the type of behavior observed by Zhen et al. for BIC's of a TM-like mode in a 1D grating.[7] Also note that the coincidence of the two vortices at the Γ-point is related to the Kerker condition mentioned earlier.[6] Based on these results, we expect that our dipole model can be used to explain Friedrich-Wintgen BICs in other 1D and 2D structures as well. The applicability of the dipole model would depend on what the underlying resonators of the BIC are. We would expect that e.g. resonances in higher-order TE or TM branches, which can support topological charges higher than 1, could be modeled by a combination of higher-order multipoles rather than dipoles.[7]

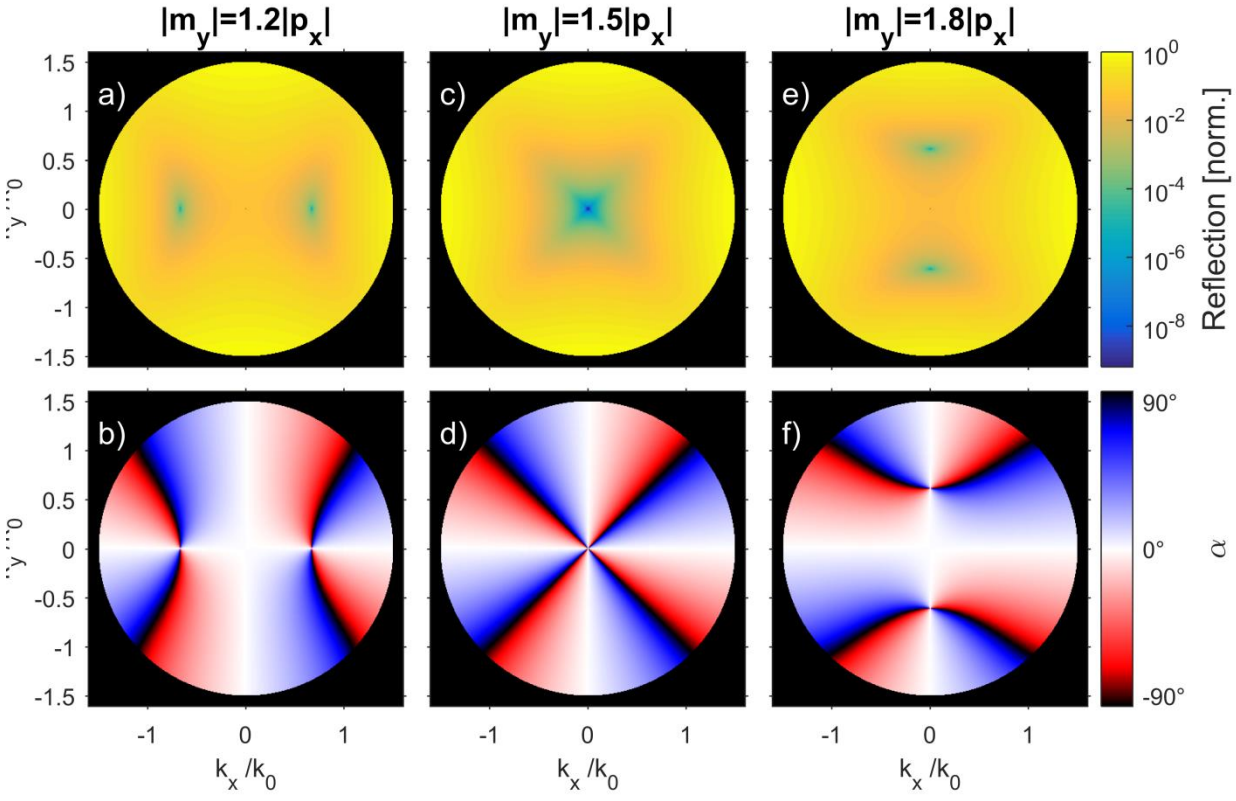

Figure S10: Charge bouncing in the dipole model. K-space images of the reflected power (top row) and polarization angle α (bottom row) from a sheet of electromagnetic dipoles. The dipoles had a nonzero electric x-polarizability α_{xx}^{p} and a magnetic y-

polarizability. We consider three different ratios of these polarizability elements: $\alpha_{yy}^{m}/\alpha_{xx}^{p} =$ -1.2 **(a-b)**, -1.5 **(c-d)** and -1.8 **(e-f)**. Going from low to high ratio, we can see the vortices move from the x-axis to the Γ-point and then bouncing to opposite sides on the y-axis.

Bibliography

1. Moharam, M. G., Gaylord, T. K., Grann, E. B. & Pommet, D. A. Formulation for stable and efficient implementation of the rigorous coupled-wave analysis of binary gratings. *J. Opt. Soc. Am. A* **12,** 1068 (1995).

2. Sersic, I., Tuambilangana, C., Kampfrath, T. & Koenderink, A. F. Magnetoelectric point scattering theory for metamaterial scatterers. *Phys. Rev. B* **83,** (2011).

3. Novotny, L. & Hecht, B. *Principles of Nano-Optics*. (Cambridge University Press, 2012).

4. Alù, A. & Engheta, N. How does zero forward-scattering in magnetodielectric nanoparticles comply with the optical theorem? *J. Nanophotonics* **4,** 41590 (2010).

5. Staude, I. *et al.* Tailoring Directional Scattering through Magnetic and Electric Resonances in Subwavelength Silicon Nanodisks. *ACS Nano* **7,** 7824–7832 (2013).

6. Kerker, M., Wang, D.-S. & Giles, C. L. Electromagnetic scattering by magnetic spheres. *J. Opt. Soc. Am.* **73,** 765 (1983).

7. Zhen, B., Hsu, C. W., Lu, L., Stone, A. D. & Soljačić, M. Topological Nature of Optical Bound States in the Continuum. *Phys. Rev. Lett.* **113,** 257401 (2014).

8. García de Abajo, F. J. Colloquium : Light scattering by particle and hole arrays. *Rev. Mod. Phys.* **79,** 1267–1290 (2007).